IEEE Robotics and Automation Letters (RAL) paper presented at
2024 IEEE/RSJ International Conference on Intelligent Robots and Systems (IROS)
October 14-18, 2024. Abu Dhabi, UAE

MTABot: An Efficient Morphable Terrestrial-Aerial Robot With Two Transformable Wheels

Ke Shi, Zainan Jiang, Liyan Ma, Le Qi, and Minghe Jin

***Abstract*—Terrestrial-aerial robots, capable of swift aerial navigation and enduring terrestrial operations, possess significant potential for utilization in exploration and rescue missions. However, achieving their capability to negotiate diverse terrains with a high-power-efficient structure remains a formidable challenge. This letter presents a morphable terrestrial-aerial robot, named MTABot, which achieves three modalities through the deployment of two multifunctional appendages. These include: 1) rolling mode, 2) climbing mode, both achieved with transformable two-wheeled configuration, and 3) flying mode, achieved with a bicopter configuration. Moreover, the radius and sector angle of transformable wheel have been optimized to enhance the obstacle-climbing capability; the position of the robot's body center of gravity has been optimized to balance ground gripping capacity and flight dynamic response speed. Finally, the robot's multi-terrain overcoming capability is validated through obstacle-climbing experiments and continuous terrestrial-aerial transformation experiments, and the high power efficiency of robot is affirmed, demonstrating feasibility of the design.**

***Index Terms*—Aerial systems: Mechanics and control, mechanism design, multimodal locomotion, terrestrial-aerial robot.**

I. Introduction

TERRESTRIAL-AERIAL robots exhibit considerable promise for application in domains such as disaster relief and resource exploration. These robots, integrating the advantages of unmanned aerial vehicles (UAVs) and ground vehicles, possess the ability to swiftly traverse aerial spaces, overcome obstacles, and perform prolonged tasks on terrestrial terrains.

Academic researchers have pioneered the development of a diverse array of terrestrial-aerial robots. Presently, these terrestrial-aerial robots can be broadly classified into two predominant categories: those that are based on passive wheels [1], [2], [3], [4], [5], [6], [7], and those that incorporate active terrestrial mechanisms [8], [9], [10], [11], [12], [13], [14], [15], [16].

Manuscript received 21 September 2023; accepted 22 December 2023. Date of publication 4 January 2024; date of current version 16 January 2024. This letter was recommended for publication by Associate Editor M. W. Mueller and Editor G. Loianno upon evaluation of the reviewers' comments. This work was supported by Collective Intelligence and Collaboration Laboratory under Grant QXZ23014201. *(Corresponding author: Zainan Jiang.)*

The authors are with the State Key Laboratory of Robotics and System, Harbin Institute of Technology, Harbin 150001, China (e-mail: keshi@stu.hit.edu.cn; jiangzainan@hit.edu.cn; brox@hit.edu.cn; ql85245600@126.com; mhjin@hit.edu.cn).

This letter has supplementary downloadable material available at https://doi.org/10.1109/LRA.2024.3349962, provided by the authors.

Digital Object Identifier 10.1109/LRA.2024.3349962

Robots equipped with passive wheels are structurally simple. However, they encounter challenges in rough terrains and demonstrate low energy efficiency during terrestrial locomotion. A classic example is the HyTAQ [1] configuration, which features a rolling cage installed on the exterior of a quadrotor drone. It utilizes the same actuators and control system for both flight and ground modes. Subsequent designs of robots with passive wheels have drawn inspiration from the HyTAQ. This has given rise to variations such as a robot in which each rotor is individually encapsulated within a passive frame [4], a robot based on a bicopter design [5], and a robot using omnidirectional wheels [7]. As previously mentioned, this type of robot exhibits several common drawbacks. Firstly, they struggle to operate in rough terrains due to the difficulties their passive frames face in finding stable support on uneven ground. They often experience unpredictable collisions, which result in a loss of control over the robot. Secondly, the energy efficiency of rotor-driven ground movement is inferior to that of active wheel or leg-driven mechanisms. Moreover, the use of propellers near the ground stirs up dust, impairing visibility. This could eventually cause visual sensor failure, compromising the robot's search operations.

Robots that utilize active terrestrial mechanisms exhibit enhanced adaptability in unstructured environments and demonstrate increased efficiency in terrestrial locomotion. However, these robots face a decrease in power efficiency during aerial locomotion due to their structural redundancy. Scholars propose that robots equipped with multifunctional appendages can demonstrate robust motion capabilities and environmental adaptability. These robots are capable of generating various motion modes by utilizing the same motion mechanism in different ways. One such example is a robot named M4, which utilizes four multifunctional appendages for versatile locomotion [14]. M4 can negotiate unstructured environments, including land and air. Its multifunctional appendages can function as wheels, thrusters, and legs, enabling various locomotion modes. Another example is the SPIDAR, which also utilizes four multifunctional appendages [15]. SPIDAR is a novel air-ground quadrupedal robot. It features spherically vectorable rotors distributed in each leg linkage, enabling both walking motion and transformable flight. Nonetheless, these robots have designs and system structures that are often seen as redundant and complex. These factors have hindered their widespread application.

In conclusion, existing terrestrial-aerial robots have not yet demonstrated the ability to maintain an energy-optimized structure while simultaneously navigating through unstructured

2377-3766 © 2024 IEEE. Personal use is permitted, but republication/redistribution requires IEEE permission.
See https://www.ieee.org/publications/rights/index.html for more information.

Copyright ©2024 IEEE

Authorized licensed use limited to: Harbin Institute of Technology. Downloaded on March 26,2024 at 02:09:48 UTC from IEEE Xplore. Restrictions apply.

Fig. 1. Morphable terrestrial-aerial robot. (a) Configuration of rolling mode. (b) Configuration of climbing mode. (c) Configuration of flying mode.

environments. To address this, our study utilized a design combining transformable wheels and a bicopter setup. Previous research has separately proven these two configurations to be efficient in ground movement and flight scenarios, respectively [17], [18].

This letter introduces a novel morphable terrestrial-aerial robot, named MTABot, as depicted in Fig. 1. The MTABot employs just two multifunctional appendages, enabling three distinct modes of locomotion: rolling, climbing, and flying. These appendages showcase their versatility in different modes. In both rolling and climbing modes, they function as transformable wheels. In flying mode, they operate as a bicopter. The robot's rolling mode allows for swift traversal of flat terrain, the climbing mode overcomes rough terrain, and the flying mode enables crossing over large obstacle terrain.

MTABot adopts a "pusher" configuration for its flying mode, positioning the body center of gravity (BCoG) above and the servo below. This design is intended to convert the flight pitch motion into a minimum phase system [19], which simplifies control. Furthermore, it prevents disruption of rotor airflow by the body structure.

The primary contributions of this letter are as follows:

1) A tri-modal morphable terrestrial-aerial robot configuration, equipped with transformable wheels and a bicopter setup, has been designed.
2) Parameters of wheel radius, sector angle, and wheel axis offset relative to BCoG have been optimized to enhance the robot's climbing ability and land-air maneuverability.
3) Experiments on stair-climbing and terrestrial-aerial transformation validate MTABot's ability to overcome multiple terrains and confirm its high power efficiency.

II. Design and Optimization

MATBot is composed of a main body and two multifunctional appendages. It utilizes a symmetrical layout. The total mass is approximately 2.2 kg. The structure is illustrated in Fig. 2.

Each multifunctional appendage comprises a transformable wheel, a rotor mounted on the wheel, and other connecting and transmission mechanisms. Appendage actuated by three motors: a unified motor, a transform motor, and a propeller motor. The unified motor dual-functions as wheel and flight rudder driver,

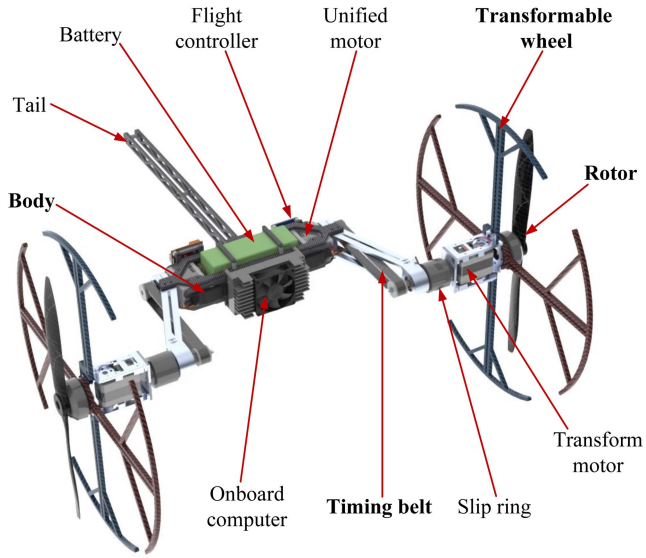

Fig. 2. Comprehensive structural diagram of the robot.

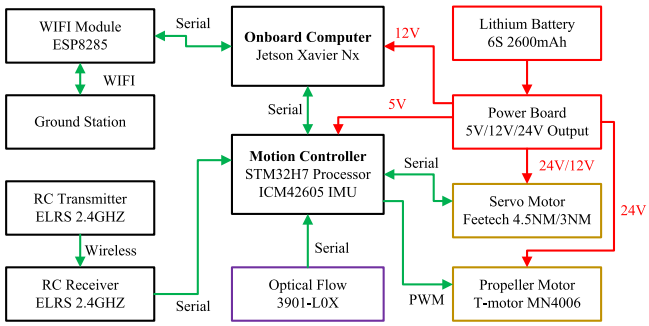

Fig. 3. Electrical architecture of MTABot, where the green lines represent logic circuits, and the red lines denote power circuits.

aiming to minimize motor usage. The transform motor facilitates mode transformation, and the propeller motor drives the rotor.

The body of the robot is equipped with electrical components such as a battery, main controller, motion controller, and motor driver. The tail rod is affixed to the body, providing support and a counterforce when the robot negotiates obstacles or uneven surfaces.

Authorized licensed use limited to: Harbin Institute of Technology. Downloaded on March 26,2024 at 02:09:48 UTC from IEEE Xplore. Restrictions apply.

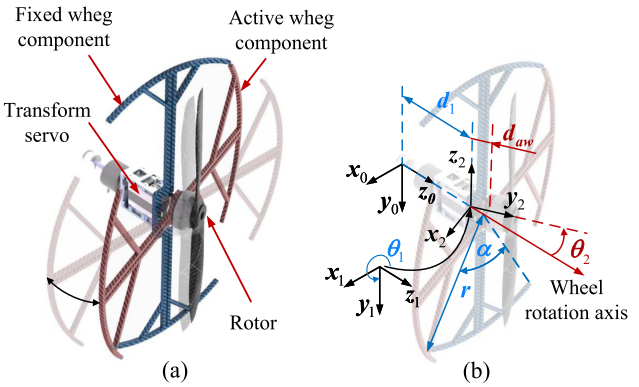

Fig. 4. Structural diagram of the robot's transformable wheel. (a) Composition of the transformable wheel. (b) Definitions of Coordinate frames and symbols, where frame $\{0\}$ is attached to the robot's body, located at the wheel joint; frame $\{1\}$ is attached to the fixed wheg, located at the joint connecting fixed wheg and active wheg; frame $\{2\}$ is attached to the active wheg, and its origin coinciding with that of frame $\{1\}$.

Fig. 3 shows MTABot's electrical architecture. Powered by a 22.2 V lithium battery with a power management module, it uses an STM32H743 ARM microcontroller with an integrated IMU chip for multimodal motion control. The main controller is a Jetson Xavier NX module, equipped with a WiFi module for remote signals and an optical flow chip for flight positioning. Propulsion comes from two T-motor Antigravity MN4006 motors (1.65 kg thrust each). The unified and transform motors are Feetech SM45BL and STS3235, respectively.

A. Design and Optimization of Transformable Wheel

MTABot employs a novel design of transformable wheel, as depicted in Fig. 4. The optimization target parameters are the radius of the wheel r and the sector angle α of the fixed wheg component.

The transformable wheel is segmented into two "wheg" components: a fixed wheg, affixed relative to the wheel axle, and an active wheg, driven by transform motor at the axle's center. This arrangement allows the wheel to switch from a standard circular form to a claw-equipped, non-standard shape, assisting the robot's transformation from rolling to climbing mode. This unique wheel design is capable of overcoming obstacles. The underlying principle is documented in [20].

The theoretical maximum height $h_{\max}$ that the transformable wheel can climb is expressed as follows:

$$h_{max} = r + r \cdot \cos\left(\frac{\alpha}{2}\right), \quad 0 < \alpha < \pi \tag{1}$$

The stair riser code is up to 178 mm (7 inches), denoted as r_0, referring to the International Code Council (ICC). For the transformable wheel to navigate most steps, it must meet the condition $2r \geq r_0$. Given the wheel's advantage of overcoming obstacles larger than its radius and the constraint to minimize dimensions, we set $r \leq r_0$. The design objective for this transformable wheel is to traverse obstacles 1.2 times its radius. The constraints are summarized as follows:

$$\frac{r_0}{2} \leq r \leq r_0 \tag{2}$$

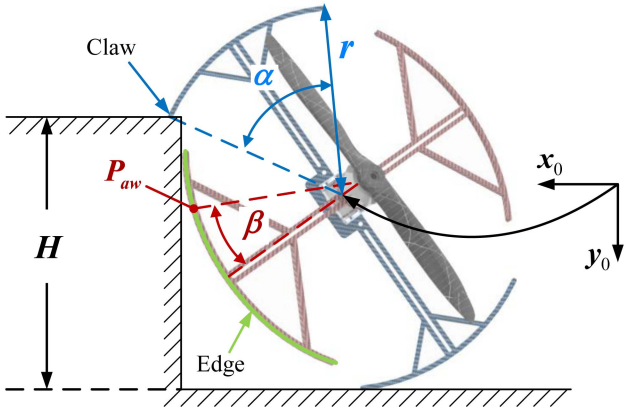

Fig. 5. Principle underlying the stair-climbing capability of the transformable wheel.

$$r + r \cdot \cos\left(\frac{\alpha}{2}\right) \geq 1.2r \tag{3}$$

Each transformable wheel possesses two degrees of freedom (2 DoF), denoted by θ_1 (wheel's rotation angle) and θ_2 (active wheg's rotation angle). Coordinate frames are established, as shown in Fig. 4(b). The homogeneous transformation matrix from frame $\{2\}$ to $\{0\}$ is computed as in (4), where $\mathrm{s}\theta$ and $\mathrm{c}\theta$ represent $\sin(\theta)$ and $\cos(\theta)$ respectively.

$${}^0_2\boldsymbol{T} = \begin{bmatrix} \mathrm{c}\theta_1\mathrm{c}\theta_2 & -\mathrm{c}\theta_1\mathrm{s}\theta_2 & \mathrm{s}\theta_1 & 0 \\ \mathrm{c}\theta_2\mathrm{s}\theta_1 & -\mathrm{s}\theta_1\mathrm{s}\theta_2 & -\mathrm{c}\theta_1 & 0 \\ \mathrm{s}\theta_2 & \mathrm{c}\theta_2 & 0 & d_1 \\ 0 & 0 & 0 & 1 \end{bmatrix} \tag{4}$$

As shown in Fig. 5, $\boldsymbol{p_{aw}}$ represents a point on the edge of the active wheg. By integrating information from Figs. 4 and 5, these points can be expressed in the $\{2\}$ coordinate system as ${}^2\boldsymbol{p_{aw}} = [r\cos(\beta), d_{aw}, r\sin(\beta)]^{\mathrm{T}}$. The corresponding coordinates in the $\{0\}$ coordinate system, noted as ${}^0\boldsymbol{p_{aw}}$, are expressed as:

$$\begin{bmatrix} {}^0\boldsymbol{p_{aw}} \\ 1 \end{bmatrix} = {}^0_2\boldsymbol{T} \begin{bmatrix} {}^2\boldsymbol{p_{aw}} \\ 1 \end{bmatrix} \tag{5}$$

Substituting into (4), we obtain:

$${}^0\boldsymbol{p_{aw}} = \begin{bmatrix} r\mathrm{s}\beta\mathrm{s}\theta_1 + r\mathrm{c}\beta\mathrm{c}\theta_1\mathrm{c}\theta_2 - d_{aw}\mathrm{c}\theta_1\mathrm{s}\theta_2 \\ r\mathrm{c}\beta\mathrm{c}\theta_2\mathrm{s}\theta_1 - r\mathrm{s}\beta\mathrm{c}\theta_1 - d_{aw}\mathrm{s}\theta_1\mathrm{s}\theta_2 \\ d_{aw}\mathrm{c}\theta_2 + r\mathrm{c}\beta\mathrm{s}\theta_2 + d_1 \end{bmatrix} \tag{6}$$

where $\beta \in [\frac{\alpha-\pi}{2}, \frac{\pi-\alpha}{2}] \cup [\frac{\pi+\alpha}{2}, \frac{3\pi-\alpha}{2}]$.

The climbing principle of transformable wheel is illustrated in Fig. 5, where H represents the height of the obstacle. For successful stair climbing, it is crucial that the maximum x_0 coordinate of the edge of the active wheg component is less than the x_0 coordinate of the claw on the fixed wheg component. Considering obstacles' rounded corners, the design should maximize this coordinate difference. To optimize the robot's stair-climbing success rate, a design optimization function (7) is established. Here, ${}^0\boldsymbol{p_{aw}}(1)$ represents the first element of ${}^0\boldsymbol{p_{aw}}$.

$$f_{w1} = r\sin\left(\theta_1 + \frac{\alpha}{2}\right) - \max\left({}^0\boldsymbol{p_{aw}}(1)\right) \tag{7}$$

Authorized licensed use limited to: Harbin Institute of Technology. Downloaded on March 26,2024 at 02:09:48 UTC from IEEE Xplore. Restrictions apply.

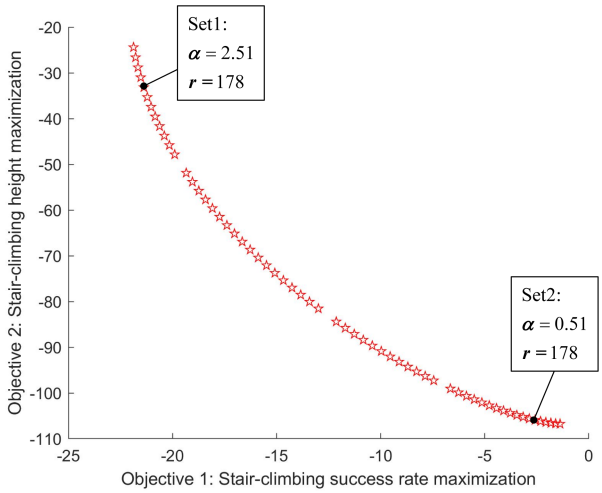

Fig. 6. Pareto Front for transformable wheel optimization, with optimal variables α (rad) and r (mm).

To maximize the climbing height, another optimization function is designed as follows:

$$f_{w2} = r + r \cdot \cos\left(\frac{\alpha}{2}\right) \tag{8}$$

The objective is to maximize f_{w1} and f_{w2}, combining them with weights λ_{w1} and λ_{w2} to form the following objective function:

$$f_{w0} = -\lambda_{w1} f_{w1} - \lambda_{w2} f_{w2} \tag{9}$$

Under the constraint condition that the robot overcomes an obstacle of height $1.2r$, the maximum sector angle of the fixed component is set as $\alpha_{\max}$. In this case, $\alpha_{\max} = 2\theta_1 + \alpha$. Based on this, (7)–(9) can be reconstructed into the following optimization problem:

$$\begin{aligned} \underset{\alpha,r}{\text{minimize}} \quad & f_{w0} \\ \text{subject to} \quad & \frac{r_0}{2} \le r \le r_0 \\ & r + r \cdot \cos\left(\frac{\alpha}{2}\right) \ge 1.2r \\ & \theta_1 = \frac{\alpha_{max} - \alpha}{2} \\ & \frac{\alpha - \pi}{2} \le \beta \le \frac{\pi - \alpha}{2} \end{aligned} \tag{10}$$

Adopting $\lambda_{w1} = 0.4$ and $\lambda_{w2} = 0.6$, we prioritize maximum climbing height over stair-climbing success rate. Given the constraints of the robot's body and wheel axle dimensions, the model sets $d_{aw} = 22$ mm, and θ_2 to a maximum of 0.70 rad. Utilizing these constraints, a genetic algorithm (GA) iteratively identifies non-dominated points in the objective space, leading to the generation of a Pareto Front.

Fig. 6 depicts the Pareto Front, revealing the trade-off between two objectives through 60 optimal points. It shows a consistent convergence of the radius r to its upper limit, while α is almost freely selectable within the constraint space. For robustness, we adopt the median values from the search results: $\alpha = 1.32$ rad and $r = 178$ mm.

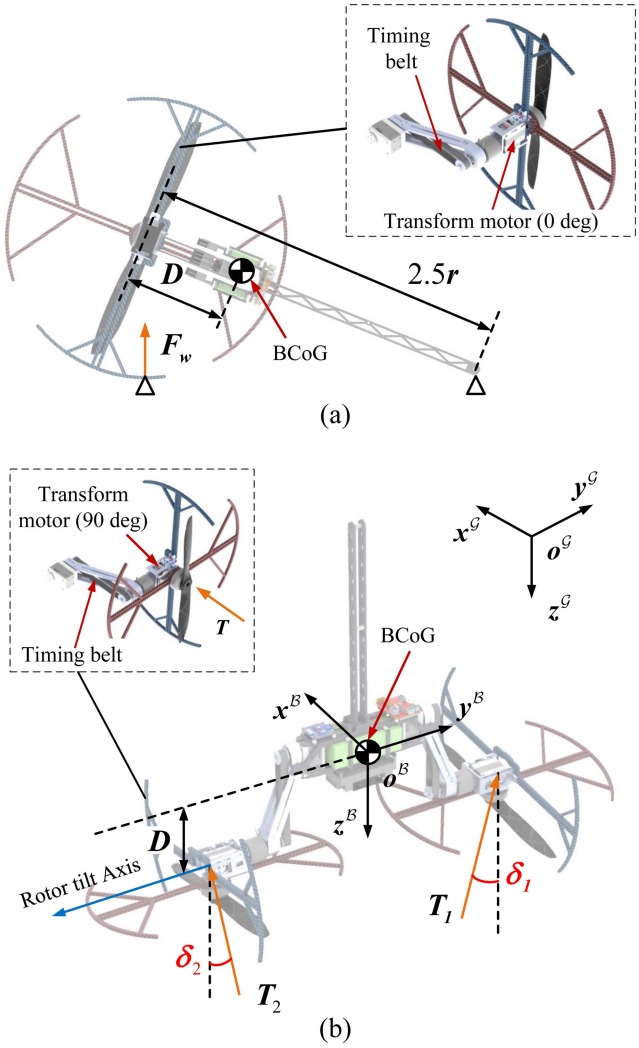

Fig. 7. Configuration diagrams of the robot's rolling and flying modes. (a) Definitions of symbols in rolling mode. (b) Definitions of coordinates and symbols in flying mode.

Considering the forced elastic deformation of whegs on uneven terrain, which can cause interference with mode transformation, the sector angle design value should be less than the optimized result. Finite element calculations under load constraint (equal to unified motor's peak torque) result in a sector angle offset of 0.20 rad. Consequently, the final sector angle is 1.62 rad for active wheg and 1.12 rad for fixed wheg.

B. Design and Optimization of Multifunctional Appendage

Fig. 2 and the dashed box in Fig. 7 depict the multifunctional appendage. The target optimization parameter is the offset of the wheel axis from BCoG, denoted as D in Fig. 7. This optimal parameter is actualized in production by adjusting the center distance of the two timing belt wheels.

Previous section introduced the composition of the multifunctional appendage. Specifically, the rotor is rigidly connected to active wheg. The transmission mechanism is mainly the timing

Authorized licensed use limited to: Harbin Institute of Technology. Downloaded on March 26,2024 at 02:09:48 UTC from IEEE Xplore. Restrictions apply.

belt mechanism driven by unified motor. The transform motor drives wheel to fold, achieving a simple transformation from land to air, as shown in the Fig. 7. During flying mode, the transform motor remains locked.

The BCoG positioning critically affects a robot's roll, climb, and fly capabilities. In two-wheeled robots, reduced wheel axis offset from the BCoG improves traction [21]. Conversely, in bicopters, an increased tilt axis offset from the BCoG enhances flight pitch motion response speed [19].

In rolling mode, as depicted in Fig. 7(a), the robot's compact size is maintained by limiting its total length $< 4r$ (the most common design approach, representing the minimum size of a quadcopter configuration). In this work, the combined length of the MTABot's body and tail rod is designed to be $2.5r$, bringing the total length to $3.5r$.

As shown in Fig. 7(a), the normal contact force between the wheel and ground, F_w, is proportional to $\frac{\mathcal{M}_b g}{2} \cdot \frac{2.5r-D}{2.5r} + \mathcal{M}_w g$, where $\mathcal{M}_b$ and $\mathcal{M}_w$ represent the body and transformable wheel masses, respectively. To enhance the robot's grip, optimization function (11) was formulated.

$$f_{b1} = \frac{(2.5r - D)\mathcal{M}_b g}{5r} + \mathcal{M}_w g \tag{11}$$

In flying mode, using Fig. 7(b), we establish the pitch rotation dynamics (12) during the robot's hover. Here, $\mathcal{I}_w$ and $\mathcal{I}_b$ denote the inertia moments of the transformable wheel and body, respectively. T is the rotor's lift, with θ and δ signifying the body's pitch and rotor's tilt angles, respectively.

$$\mathcal{I}_b \ddot{\theta} = TD \sin\delta + \mathcal{I}_w \left(\ddot{\theta} + \ddot{\delta}\right) \tag{12}$$

By performing linearization and making small angle assumptions, the simplified frequency domain dynamics equation is obtained:

$$\frac{\theta(s)}{\delta(s)} = \frac{TD + \mathcal{I}_w s^2}{(\mathcal{I}_b - \mathcal{I}_w)\, s^2} \tag{13}$$

The system under consideration exhibits zeros at $z = \pm\sqrt{\frac{TD}{\mathcal{I}_w}}i$, indicating that these zeros reside on the imaginary axis of the complex plane.

Imaginary-axis zeros establish a minimum bound for the system's closed-loop control settling time, thereby decelerating its response and inducing overshoot. This effect amplifies as these zeros approach the origin [22]. Hence, for system stability and performance optimization, it is recommended to position the zeros distant from the origin. The design of Optimization function (14) is predicated on this principle.

$$f_{b2} = \sqrt{TD/\mathcal{I}_w} \tag{14}$$

The objective is to maximize f_{b1} and f_{b2}. These two objectives are combined and assigned weights λ_{b1} and λ_{b2}, respectively, leading to the formulation of the objective function as follows:

$$f_{b0} = -\lambda_{b1} f_{b1} - \lambda_{b2} f_{b2} \tag{15}$$

Equation (11), (14), (15) can be reformulated into the following optimization problem:

$$\underset{\alpha, r}{\text{minimize}} \quad f_{b0}$$

$$\text{subject to} \quad 0 < D < 2.5r \tag{16}$$

Assigning a higher weight to rolling traction over flight dynamic performance, we use $\lambda_{w1} = 0.6$ and $\lambda_{w2} = 0.4$. Given the model parameters, we have $\mathcal{M}_b = 1.60\,\text{kg}$, $\mathcal{M}_w = 0.25\,\text{kg}$, and $\mathcal{I}_w = 0.04608\,\text{kg}\cdot\text{m}^2$. The lift in the hover state is considered a constant value, i.e., $T = (\mathcal{M}_b + 2\mathcal{M}_w)g$. With these assumptions and constraints, we can directly solve for $D = 0.778r$, which rounds to $D = 135\,\text{mm}$. This value is used for further hardware assembly.

III. Control Strategy

MTABot considers control strategies for rolling mode, climbing mode, flying mode, rolling-climbing transformation, and terrestrial-aerial transformation.

A. Rolling-Climbing Mode Control

1) Rolling and Climbing Mode: PID-based two-wheeled differential control is utilized for rolling and climbing modes. The execution of this part, being straightforward and well-established, is not elaborated further.

2) Rolling-Climbing Transformation: As shown in Fig. 4, the transformation from rolling to climbing mode is accomplished through the rotation of active wheg. Furthermore, rotation angle of active wheg can be adjusted to accommodate obstacles of different sizes. Smaller angles for smaller obstacles to enhance efficiency, while larger angles for bigger obstacles to increase overcoming capability. Due to mechanical limitations, the maximum rotation angle is 40 degrees.

B. Terrestrial-Aerial Transformation Strategy

A procedural terrestrial-aerial transformation strategy has been designed to maximize the protection of propellers and minimize the load on transform motor.

The process from transformable two-wheeled configuration to bicopter configuration is as shown in Fig. 8 (green dotted line). The procedure unfolds as follows: 1) rotate active wheg components to 90 deg, then lock transform motors; 2) advance wheels until all claws achieve ground contact; 3) unified motors perpetuate forward rotation, leveraging claws to elevate and rotate the body until the tail rod is vertical.

The process from bicopter configuration back to transformable two-wheeled configuration is as shown in Fig. 8 (blue dashed line). The procedure unfolds as follows: 1) unified motors rotate rearward, guiding the robot body and tail rod to descend; 2) sequentially stabilize one wheel and invert the other until both are fully inverted; 3) concurrent two wheels advancement elevates the robot's body; 4) the active wheg component reorients to its initial position.

C. Flying Mode Control

In conventional bicopter attitude control systems, the inertial torque of the servo rudder consistently opposes the target torque of body posture adjustment, presenting the greatest challenge in controlling a bicopter. However, this issue has been addressed

Authorized licensed use limited to: Harbin Institute of Technology. Downloaded on March 26,2024 at 02:09:48 UTC from IEEE Xplore. Restrictions apply.

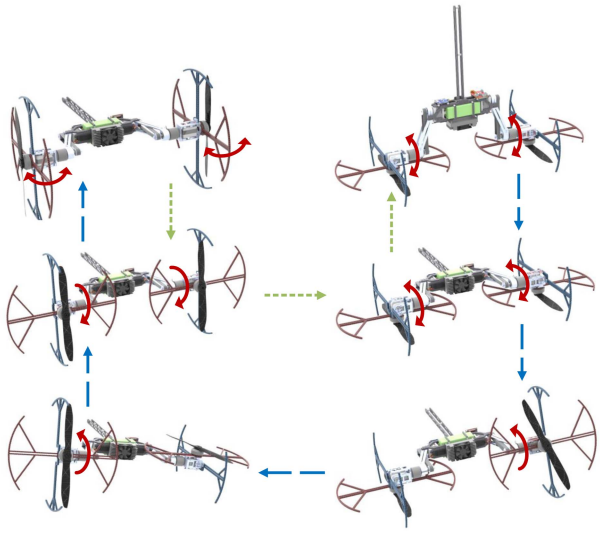

Fig. 8. Terrestrial-aerial transformation steps. The green dotted line represents land-to-air process, and the blue dashed line represents air-to-land process.

in the configuration of MTABot. That is, in the attitude control system of MTABot, the inertial torque of the servo rudder positively contributes to the control of achieving the target posture, with more details explained in Section IV of [19]. Therefore, MTABot can still use the classic single rigid body motion model to complete the controller design. The specific dynamic model, flight controller, and control allocation rules use the methods in Section IV of [18].

IV. Experiment Results

The prototype was primarily constructed from carbon fiber, with the major load-bearing structure made from aluminum alloy, as shown in the Fig. 1. In rolling mode, it measures 620 mm in length, 578 mm in width, and has a wheel diameter of 356 mm. In flying mode, the robot has a propeller shaft distance of 468 mm and a height of 530 mm.

A. Rolling-Climbing Mode Experiment

Experiments involving the MTABot's rolling mode and climbing mode were conducted in an indoor environment using remote control. The motion speed of MTABot was evaluated on a flat terrain, reaching a maximum speed of 1.35 m/s, which is comparable to the human walking speed.

As shown in Fig. 9, MTABot performed repeated climbing experiments in an indoor environment, using different active wheg rotation angles (θ_2) in two distinct conditions. In Fig. 9(a), a high obstacle with a height of 220 mm was placed, which exceeded 1.2 times the MTABot's wheel radius. Additionally, Fig. 9(b) presents a low obstacle set at 110 mm, approximately 0.6 times the MTABot's wheel radius.

Table I presents the experimental results, illustrating the MTABot's success rate in navigating obstacles of two different sizes using varying active wheg rotation angles. The success rate, expressed as $1/n$, depends on the wheel's angular displacement (set as $n\pi$) when MTABot successfully surmounts an obstacle.

TABLE I
Obstacle Climbing Success Rate (%)

Obstacle height	$\theta_2 = 10°$	$\theta_2 = 20°$	$\theta_2 = 30°$	$\theta_2 = 40°$
220 mm	-	-	25	100
110 mm	33	100	100	100

A smaller angular displacement correlates with a higher success rate, up to a maximum of 100%.

Table I demonstrate MTABot's ability to navigate obstacles of varying heights. A larger θ_2 is required for larger obstacles, while a smaller θ_2 is sufficient for smaller ones. In Fig. 9(a), MTABot uses $\theta_2 = 40°$ to overcome obstacles exceeding 1.2 times its wheel radius; in Fig. 9(b), for smaller obstacles (0.6 times its wheel radius), it employs $\theta_2 = 20°$ and a higher speed to enhance climbing efficiency, completing the entire process in under 5 seconds.

B. Terrestrial-Aerial Transformation Experiment

The experimental sequence of the robot's terrestrial-aerial transformation consists of five consecutive stages of motion. During this process, the robot will cross over an obstacle. To ensure clear visibility, the speed of the servo motor was maintained at 10% of its maximum capacity during the transformation. The experiment took place indoors, using the NOKOV motion capture system at a 60 Hz sampling frequency for data collection.

Fig. 10 presents the results of the experiment, where Fig. 10(a) depicts a freeze-frame extracted from a comprehensive motion video of the robot. To clearly illustrate the robot's pose at each stage, Fig. 10(c) and (d) have been segmented with color blocks.

The process of the robot's transformation from ground to air and back to ground is as follows:

1) Robot moves smoothly in rolling mode, corresponding to the 0:00 stage in Fig. 10(a) and the first red region in Fig. 10(c) and (d).
2) Transformation from rolling to flying, corresponding to the 0:00-0:07 stage and the green region, during which the pitch angle abruptly rotates by 111 degrees.
3) Flying mode, corresponding to the 0:12-0:17 stage in and the blue region, during which the robot's pose remains stable.
4) Transformation from flying to rolling, corresponding to the 0:23-0:38 stage and the yellow region, with the pose returning to the roll mode value.
5) Robot moves in rolling mode again, corresponding to the 0:38 stage and the second red region.

Experimental results indicate that the robot can transform from rolling mode to flying mode, and vice versa, in less than 15 seconds. When in rolling mode, the robot exhibits stability, with the fluctuation of the body's center of gravity confined to less than 2 mm. In flying mode, the robot is able to reach an equilibrium in both pose and altitude, and successfully overcomes obstacles. These results offer substantial data supporting the robot's multimodal mobility and affirm the effectiveness of the design.

Authorized licensed use limited to: Harbin Institute of Technology. Downloaded on March 26,2024 at 02:09:48 UTC from IEEE Xplore. Restrictions apply.

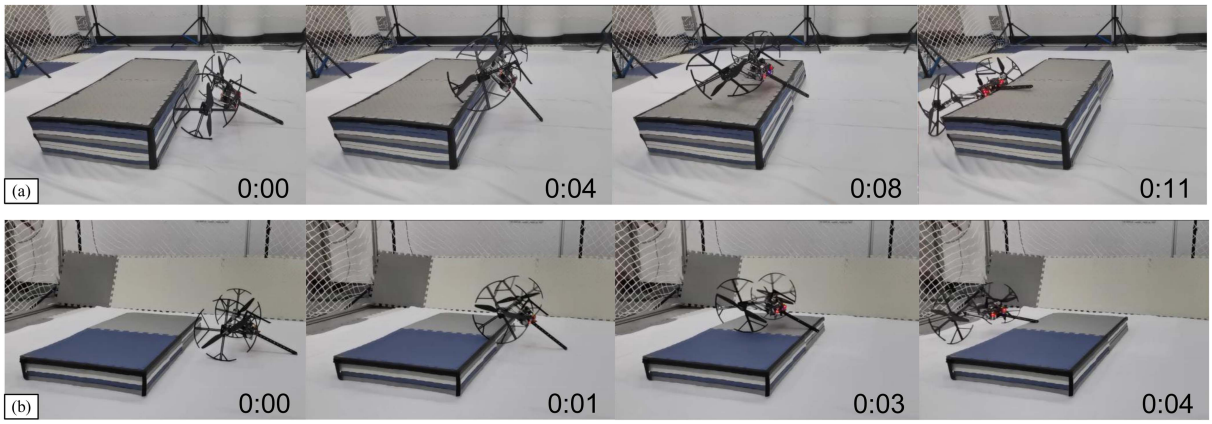

Fig. 9. Time sequence of obstacle climbing experiment. (a) High obstacle climbing experiment, with a height of 220 mm. (b) Low obstacle climbing experiment, with a height of 110 mm.

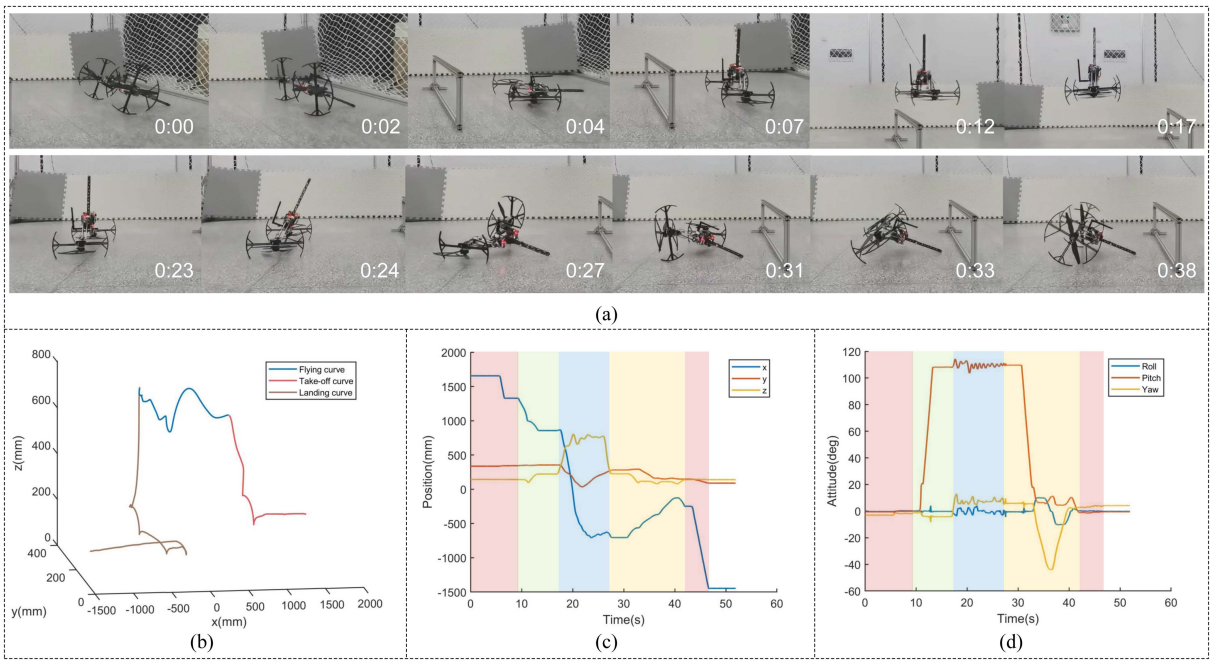

Fig. 10. Terrestrial-aerial transformation result. (a) Time sequence of terrestrial-aerial transformation. (b) 3D trajectory points corresponding to (a). (c) Position response corresponding to (a). (d) Attitude response corresponding to (a).

C. Power Efficiency Validation

The energy consumption of the MTABot was measured using a power meter. It was found that the motor consumed 9 watts of power while rolling at a speed of 1 m/s on flat terrain, and 330 watts during flight. The power efficiency of the MTABot was evaluated using the weight-to-power ratio (g/w). The results showed that on the ground and in the air, the MTABot demonstrated efficiencies of 244.44 and 6.67, respectively.

As depicted in Fig. 11, a comparative analysis with recent typical terrestrial-aerial robots, including Quadrolltor [2], SytaB [5], BogieCopter [6], Skywalker [7], LEO [12], M4 [14], and DoubleBee [16], demonstrates MTABot's superior aerial efficiency. MTABot's ground efficiency was only surpassed by DoubleBee, but the absence of speed constraints in DoubleBee's data prevents a definitive conclusion regarding its superiority over MTABot. Overall, MTABot exhibits leading energy efficiency among current terrestrial-aerial robots, highlighting its simplicity and high efficiency.

V. Conclusion and Future Work

A. Contributions

This letter presents the MTABot, a design that integrates the bicopter and the transformable wheel configuration. It combines a rotor and a transformable wheel to form a multifunctional appendage. By utilizing this appendage in three distinct ways, the MTABot is able to roll across flat terrain, climb stairs, and fly in aerial environments, respectively. Furthermore, the power

Authorized licensed use limited to: Harbin Institute of Technology. Downloaded on March 26,2024 at 02:09:48 UTC from IEEE Xplore. Restrictions apply.

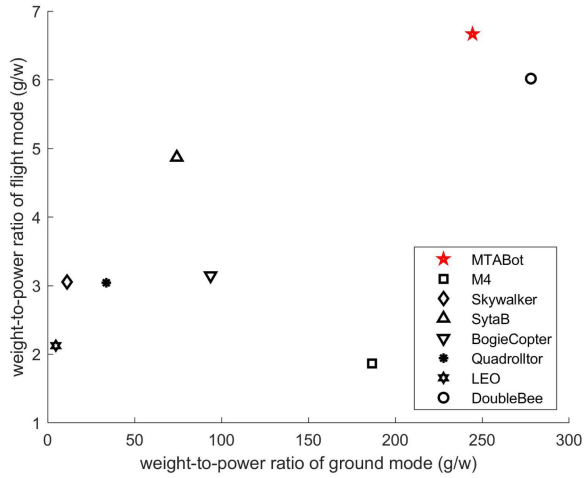

Fig. 11. Power efficiency of MTABot and other terrestrial-aerial robots.

efficiency of the MTABot has been confirmed to be superior compared to most existing terrestrial-aerial robots.

B. Potential Limitations and Future Work

The integration and debugging complexity of the MTABot surpasses that of conventional multirotors. Furthermore, in this work, the locomotion capabilities of the MTABot have not been evaluated under unpredictable real-world scenarios. Future research will explore additional locomotion modalities, such as using transform motors in flight modes, to decouple the robot's roll and translational movements for more precise operations. Subsequent work will also develop a unified planning approach that allows MTABot to adapt its configuration and trajectory based on the geometry of obstacles in an unknown real-world environment. This will enable MTABot to proactively select operational modes and plan joint motions, thereby enhancing its adaptability to complex terrains.

REFERENCES

[1] A. Kalantari and M. Spenko, "Design and experimental validation of HyTAQ, A hybrid terrestrial and aerial quadrotor," in *Proc. IEEE Int. Conf. Robot. Automat.*, Karlsruhe, Germany, 2013, pp. 4445–4450.

[2] H. Jia, R. Ding, K. Dong, S. Bai, and P. Chirarattananon, "Quadrolltor: A reconfigurable quadrotor with controlled rolling and turning," *IEEE Robot. Automat. Lett.*, vol. 8, no. 7, pp. 4052–4059, Jul. 2023.

[3] S. Mizutani, Y. Okada, C. J. Salaan, T. Ishii, K. Ohno, and S. Tadokoro, "Proposal and experimental validation of a design strategy for a UAV with a passive rotating spherical shell," in *Proc. IEEE/RSJ Int. Conf. Intell. Robots Syst.*, Hamburg, Germany, 2015, pp. 1271–1278.

[4] C. J. Salaan, K. Tadakuma, Y. Okada, Y. Sakai, K. Ohno, and S. Tadokoro, "Development and experimental validation of aerial vehicle with passive rotating shell on each rotor," *IEEE Robot. Automat. Lett.*, vol. 4, no. 3, pp. 2568–2575, Jul. 2019.

[5] J. Yang, Y. Zhu, L. Zhang, Y. Dong, and Y. Ding, "SytaB: A class of smooth-transition hybrid terrestrial/aerial bicopters," *IEEE Robot. Automat. Lett.*, vol. 7, no. 4, pp. 9199–9206, Oct. 2022.

[6] T. Dias and M. Basiri, "BogieCopter: A multi-modal aerial-ground vehicle for long-endurance inspection applications," in *Proc. IEEE Int. Conf. Robot. Autom.*, 2023, pp. 3303–3309.

[7] N. Pan, J. Jiang, R. Zhang, C. Xu, and F. Gao, "Skywalker: A compact and agile air-ground omnidirectional vehicle," *IEEE Robot. Automat. Lett.*, vol. 8, no. 5, pp. 2534–2541, May 2023.

[8] S. Mintchev and D. Floreano, "A multi-modal hovering and terrestrial robot with adaptive morphology," in *Proc. 2nd Int. Symp. Aerial Robot.*, 2018.

[9] Q. Tan, X. Zhang, H. Liu, S. Jiao, M. Zhou, and J. Li, "Multi-modal dynamics analysis and control for amphibious fly-drive vehicle," *IEEE/ASME Trans. Mechatron.*, vol. 26, no. 2, pp. 621–632, Apr. 2021.

[10] N. B. David and D. Zarrouk, "Design and analysis of FCSTAR, a hybrid flying and climbing sprawl tuned robot," *IEEE Robot. Automat. Lett.*, vol. 6, no. 4, pp. 6188–6195, Oct. 2021.

[11] A. Kalantari et al., "Drivocopter: A concept hybrid aerial/ground vehicle for long-endurance mobility," in *Proc. IEEE Aerosp. Conf.*, Big Sky, MT, USA, 2020, pp. 1–10.

[12] K. Kim, P. Spieler, E.-S. Lupu, A. Ramezani, and S.-J. Chung, "A bipedal walking robot that can fly, slackline, and skateboard," *Sci. Robot.*, vol. 6, no. 59, Oct. 2021, Art. no. eabf8136.

[13] N. Meiri and D. Zarrouk, "Flying STAR, a hybrid crawling and flying sprawl tuned robot," in *Proc. Int. Conf. Robot. Automat.*, 2019, pp. 5302–5308.

[14] E. Sihite, A. Kalantari, R. Nemovi, A. Ramezani, and M. Gharib, "Multi-modal mobility morphobot (M4) with appendage repurposing for locomotion plasticity enhancement," *Nature Commun.*, vol. 14, no. 1, Jun. 2023, Art. no. 3323.

[15] M. Zhao, T. Anzai, and T. Nishio, "Design, modeling, and control of a quadruped robot SPIDAR: Spherically vectorable and distributed rotors assisted air-ground quadruped robot," *IEEE Robot. Automat. Lett.*, vol. 8, no. 7, pp. 3923–3930, Jul. 2023.

[16] M. Cao, X. Xu, S. Yuan, K. Cao, K. Liu, and L. Xie, "DoubleBee: A hybrid aerial-ground robot with two active wheels," in *Proc. IEEE/RSJ Int. Conf. Intell. Robots Syst.*, Oct. 2023, pp. 6962–6969.

[17] C. Zheng, S. Sane, K. Lee, V. Kalyanram, and K. Lee, "α-WaLTR: Adaptive wheel-and-leg transformable robot for versatile multiterrain locomotion," *IEEE Trans. Robot.*, vol. 39, no. 2, pp. 941–958, Apr. 2023.

[18] Y. Qin, W. Xu, A. Lee, and F. Zhang, "Gemini: A compact yet efficient bi-copter UAV for indoor applications," *IEEE Robot. Automat. Lett.*, vol. 5, no. 2, pp. 3213–3220, Apr. 2020.

[19] X. He and Y. Wang, "Design and trajectory tracking control of a new bi-copter UAV," *IEEE Robot. Automat. Lett.*, vol. 7, no. 4, pp. 9191–9198, Oct. 2022.

[20] G. Zhang, S. Ma, J. Liu, X. Zeng, L. Kong, and Y. Li, "Q-whex: A simple and highly mobile quasi-wheeled hexapod robot," *J. Field Robot.*, vol. 40, pp. 1444–1459, 2023.

[21] A. Salerno and J. Angeles, "A new family of two-wheeled mobile robots: Modeling and controllability," *IEEE Trans. Robot.*, vol. 23, no. 1, pp. 169–173, Feb. 2007.

[22] G. C. Goodwin, S. F. Graebe, and M. E. Salgado, *Control System Design*. Hoboken, NJ, USA: Prentice Hall, 2000.

Authorized licensed use limited to: Harbin Institute of Technology. Downloaded on March 26,2024 at 02:09:48 UTC from IEEE Xplore. Restrictions apply.